Tellus SERIES B CHEMICAL AND PHYSICAL METEOROLOGY
PUBLISHED BY THE INTERNATIONAL METEOROLOGICAL INSTITUTE IN STOCKHOLM

Tellus (2011), 63B, 459–474
Printed in Singapore. All rights reserved

Ground-based off-line aerosol measurements at Praia, Cape Verde, during the Saharan Mineral Dust Experiment: microphysical properties and mineralogy

By K. KANDLER[1]*, L. SCHÜTZ[2], S. JÄCKEL[1], K. LIEKE[1], C. EMMEL[2], D. MÜLLER-EBERT[1], M. EBERT[1], D. SCHEUVENS[1,2], A. SCHLADITZ[3], B. ŠEGVIĆ[1], A. WIEDENSOHLER[3] and S. WEINBRUCH[1], [1]*Institut für Angewandte Geowissenschaften, Technische Universität Darmstadt, Schnittspahnstr. 9, 64287 Darmstadt, Germany;* [2]*Institut für Physik der Atmosphäre, Johannes-Gutenberg-Universität, J.-J.-Becherweg 21, 55099 Mainz, Germany;* [3]*Leibniz-Institut für Troposphärenforschung, Permoserstr. 15, 04318 Leipzig, Germany*

(Manuscript received 13 October 2010; in final form 2 May 2011)

ABSTRACT

A large field experiment of the Saharan Mineral Dust Experiment (SAMUM) was performed in Praia, Cape Verde, in January and February 2008. This work reports on the aerosol mass concentrations, size distributions and mineralogical composition of the aerosol arriving at Praia. Three dust periods were recorded during the measurements, divided by transitional periods and embedded in maritime-influenced situations. The total suspended particle mass/PM_{10}/$PM_{2.5}$ were 250/180/74 $\mu g/m^3$ on average for the first dust period (17–21 January) and 250/230/83 $\mu g/m^3$ for the second (24–26 January). The third period (28 January to 2 February) was the most intensive with 410/340/130 $\mu g/m^3$. Four modes were identified in the size distribution. The first mode (50–70 nm) and partly the second (700–1100 nm) can be regarded as of marine origin, but some dust contributes to the latter. The third mode (2–4 μm) is dominated by advected dust, while the intermittently occurring fourth mode (15–70 μm) may have a local contribution. The dust consisted of kaolinite (dust/maritime period: 35%wt./25%wt.), K-feldspar (20%wt./25%wt.), illite (14%wt./10%wt.), quartz (11%wt./8%wt.), smectites (6%wt./4%wt.), plagioclase (6%wt./1%wt.), gypsum (4%wt./7%wt.), halite (2%wt./17%wt.) and calcite (2%wt./3%wt.).

1. Introduction

Saharan dust has attracted increasing attention since the 1960s because of its importance as one major component of the global aerosol burden, comparable in mass to the sea-salt load (Junge, 1979). On a global scale dust influences the earth radiation budget by influencing radiative transfer (Carlson and Benjamin, 1980; Tegen, 2003; Mahowald et al., 2006; Jeong and Sokolik, 2007) and by influencing the cloud microphysics by different pathways (DeMott et al., 2003; Andreae and Rosenfeld, 2008; Zimmermann et al., 2008). On a more regional scale it can provide nutrients to oceanic and continental ecosystems (Jickells et al., 2005; Koren et al., 2006).

The overall perspective of the Saharan Mineral Dust Experiment (SAMUM) is to characterize the Saharan mineral dust especially in view of its radiative properties. While the first part of SAMUM aimed at the characterization of pristine Saharan mineral dust, resulting in a field campaign in southeast Morocco (Heintzenberg, 2009), the second phase of SAMUM is dedicated to the investigation of possible alterations of transported mineral dust, of modifications to the aerosol due to admixture of non-dust aerosols like sea–salt or biomass burning particles, and of changes due to other dust sources and varying transport regime. For this reason, the second SAMUM field campaign was performed in and over the Cape Verde region west of Africa (Ansmann et al., 2011). This first part on off-line aerosol measurements at the SAMUM ground station at Praia, Cape Verde, presents results on aerosol microphysics with emphasis on the large particle size range and on dust mineralogy.

The tropical Northern Atlantic Ocean is located under the pathway of Saharan dust, which is transported across the ocean towards the Caribbean Sea (e.g. Prospero, 1999; Reid et al., 2003; Chiapello et al., 2005; Muhs et al., 2007) and into the Amazonian region (e.g. Prospero et al., 1981; Formenti et al., 2001). The isotopic composition of deep sea sediments east of the Middle Atlantic ridge shows by strong signatures of

*Corresponding author.
Institut für Angewandte Geowissenschaften, Technische Universität Darmstadt, Schnittspahnstr. 9, 64287 Darmstadt, Germany.
e-mail: kzk@gmx.de
DOI: 10.1111/j.1600-0889.2011.00546.x

long-term inputs that North African windblown soil material is transported over the Atlantic Ocean since pre-historical times (e.g. Biscaye et al., 1974; Grousset et al., 1988; Grousset et al., 1992; Rognon et al., 1996). Dust fallout onto merchant vessels cruising off the West African coast and in major parts of the trade wind region is well known since historical times (Darwin, 1846). On board of the research vessel Meteor cruising west of the African coastline Saharan mineral dust was measured in the size range of 0.4 μm $< d <$ 40 μm (Junge and Jaenicke, 1971).

The horizontal and vertical distribution of the Saharan air layer (SAL) over the tropical North Atlantic was documented by a multitude of works (e.g. Carlson and Prospero, 1972; Prospero and Carlson, 1972; Karyampudi et al., 1999). Their findings are well confirmed in a comprehensive study by Huang et al. (2010) using Aqua-MODIS aerosol optical depth and CALIPSO lidar satellite data together with NCEP reanalysis temperature and 3D wind field data, which also the seasonal shift of the Saharan air and dust layer over the subtropical North Atlantic Ocean is well documented.

2. Measurement Location

The Cape Verde Islands are located in an area with a year-round dust aerosol appearance in the pathway of the largest Saharan dust sources (Middleton and Goudie, 2001). During the summer season, a dust layer extending from above the marine boundary layer on the order of 500 m up to altitudes of 5 km can be observed during heavy dust outbreaks (Huang et al., 2010). In the winter season with moderate dust activity, the SAL extends to altitudes of about 3 to 4 km. In addition during winter, Saharan dust is transported inside the marine boundary layer (Chiapello et al., 1995). This lower altitude of transport and, thus, also different main direction of transport may lead to a change in sources supplying dust to the Cape Verde Islands (Prospero, 1996). Intensive biomass burning activities in wintertime in the Sahel region contribute to the Saharan air masses emerging West Africa (Kaufman et al., 2005; Osborne et al., 2008). Thus, the columnar aerosol load is composed of sea–salt particles in the marine boundary layer and Saharan dust plus biomass burning material aloft, depending on transport conditions. The Saharan aerosol is mixed into the boundary layer through sedimentation and turbulent diffusion (Jaenicke and Schütz, 1978; Schütz et al., 1981). As the Cape Verde islands are the only land area west of Africa in the centre of the African dust plume, they have attracted a number of field experiments through the last decades (Jaenicke and Schütz, 1978; Talbot et al., 1986; Moulin et al., 1997; Caquineau et al., 1998; Ratmeyer et al., 1999a; Tanré et al., 2003; Nalli et al., 2005; Stuut et al., 2005; Ansmann et al., 2009; Zipser et al., 2009; Chen et al., 2011).

The SAMUM ground station was located on the airport of Praia, Cape Verde, at 14° 56′ 50.89″ N and 23° 29′ 4.31″ W, approximately 110 m a.s.l (Fig. 1). The distance to the airport runway was 200 m, but the air traffic density at Praia is low and no discontinuous measurements were performed during or after air plane take-off or landing. Upwind of the station follows about 7 km of coastline including three small settlements, which are located in valleys near sea level. The city of Praia is located downwind of the station, so no large anthropogenic direct influence occurred during the campaign.

Particle collection was performed on top of an aerosol measurement container, and all instruments were adjusted to a sampling altitude of 4 m above ground. The container was placed at the northeast corner of the Praia station to avoid local contamination by the co-workers. For the same reason, the upwind sector of the aerosol measurement container was kept free of personal traffic to avoid a soil disturbance. Meteorological data sets were also acquired at 4 m above ground on top of the aerosol measurement container.

3. Measurement techniques

Meteorological data were acquired with a time resolution of 1 min. Temperature and relative humidity were measured by a Humicap sensor (HMP233, Vaisala, Vantaa, Finland). Wind speed and direction were recorded by a three-dimensional ultrasonic anemometer (Model 81000, R. M. Young, Traverse City, Michigan, USA). Air pressure was taken at station level with a precision barometric sensor (type 5002.0000, Friedrichs, Schenefeld, Germany). Soil temperature was measured with two standard Pt100 sensors. Data acquisition was performed by three digital loggers (Combilog 1020, Friedrichs, Schenefeld, Germany), averaging measurements over 1 min.

Mass concentrations were measured by gravimetry. Aerosol was collected on glass fibre filters (MN GF-5, Macherey & Nagel, Düren, Germany). To minimize inlet and transmission losses, total suspended particle matter (TSP) was collected with a quasi-isokinetic, iso-axially operated filter sampler on a wind vane. PM_{10}- and $PM_{2.5}$-equivalent aerosol was collected by using glass fiber filters behind an impactor with a 50% sampling efficiency at 10 μm and 2.5 μm aerodynamic particle diameter, respectively. This set up was nearly identical to the one during SAMUM-1 in Tinfou, Morocco (see also Kandler et al., 2009), except that during SAMUM-1 instead of the $PM_{2.5}$-equivalent a $PM_{2.3}$-equivalent was sampled. The air mass flow was measured continuously with a set of mass flow meters (Mass-Stream D-6250, Bronkhorst Mättig, Unna, Germany) and converted to a volume flow at 1013 hPa and 273.25 K. The filters were weighted at approximately 50% relative humidity with a micro-balance (model CP225D, Sartorius, Göttingen, Germany) before and after sampling. The weighing error is estimated as 100 μg, which converts to an uncertainty in mass concentration for $PM_{2.5}$ equivalent between 0.5 and 18% (average 2%), for PM_{10} equivalent between 0.2 and 3.5% (average 0.5%), and for TSP between 0.1 and 0.8% (average 0.2%). The uncertainty in air volume determination is below 5%. Mass concentrations and sampling intervals are summarized in Table 1.

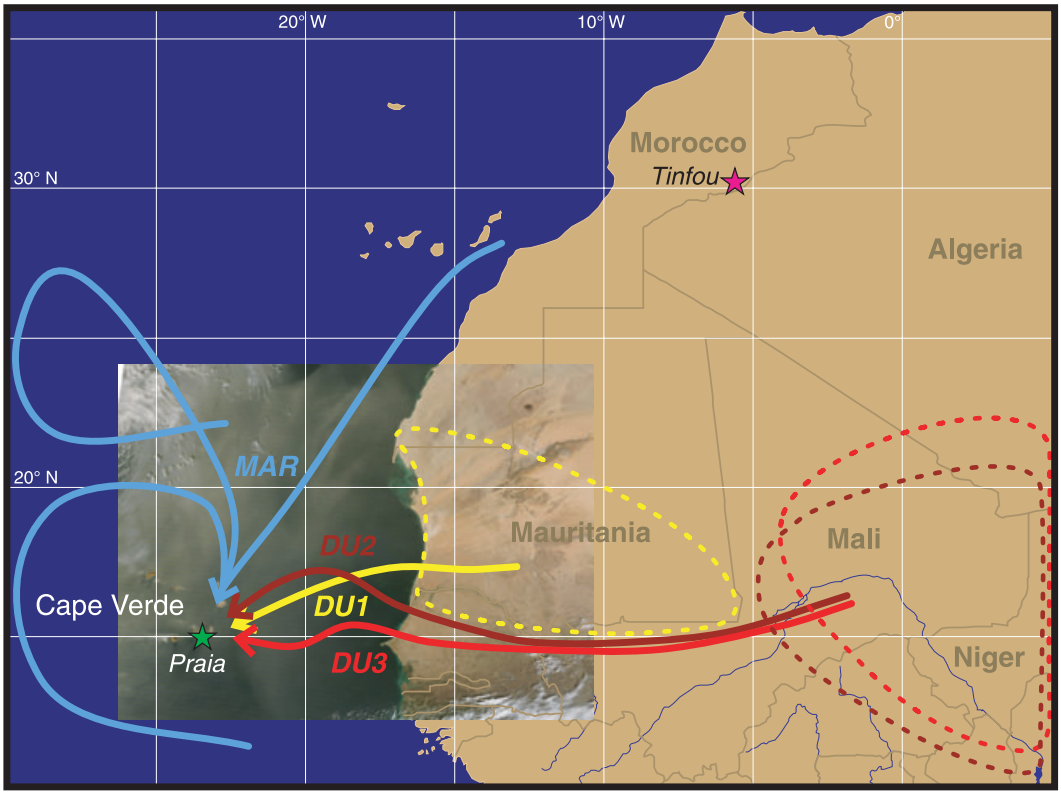

Fig. 1. Map of the measurement region. The location of the SAMUM-2 ground station at Praia, Santiago Island, Cape Verde, is marked by a green star, the location of the SAMUM-1 ground station in Tinfou, Morocco, by a magenta star. Backward trajectories for the three main dust phases (DU1, DU2, DU3, see below for details) and for the maritime phases (MAR) are shown by arrows. The most probable source regions for the three dust phases are outlined by dashed lines. The satellite image (courtesy of NASA Earth Observatory, http://earthobservatory.nasa.gov/NaturalHazards/view.php?id=19569) shows the situation during DU3 on 29 January, 2008.

The mineralogical composition of the aerosol bulk samples was determined by X-ray powder diffraction analysis (XRD). Relevant measurement parameters are shown in Table 2. Identification of the mineral phases was performed using the ICDD Database (ICDD, 2002). Relative mineral contents were calculated using the standard-less reference intensity ratio (RIR) or 'matrix-flushing' method by Chung (1974). The ICDD Database already provides RIR values of all mineral phases necessary for the quantification process. By comparison to relative mineral abundances obtained by FULLPAT (Chipera and Bish, 2002), Kandler et al. (2009) showed the reliability of the RIR approach for aerosol samples. For the XRD measurements, the filters containing the aerosol were cut into 3 cm × 3 cm pieces and mounted on a silicon wafer to reduce background contributions. It is assumed that the particles show no preferred orientation or gradation, which is required for accurate quantification (Brindley, 1980; Moore and Reynolds, 1997). Each filter was measured with copper and cobalt radiation (graphite monochromator). A cobalt X-ray tube was used to decrease the detection limits for ferrous minerals. Clay minerals were identified using textured specimens (Brindley, 1980; Moore and Reynolds, 1997). For this analysis, the aerosol was separated from the filters by ultrasonic treatment in a few millilitres of distilled water. The total content of the clay fraction (defined as the size fraction with particles smaller than 2 μm) was determined by weighing after gravitational separation in a centrifuge and drying. As single samples did not yield enough signal or the lines of clay mineral phases were masked by other minerals, an integral textured specimen was prepared for each period (DU1, DU2, DU3, MAR1 + MAR2). For the meteorological period classification see chapter 4.1 and refer to Knippertz et al. (2011). After these measurements, the three integral dust period samples were merged for a more detailed investigation of the clay minerals. To check for the presence of smectite, samples were treated with ethylene glycol. Heating to 550 °C allowed discrimination between chlorite and kaolinite. To obtain a quantitative analysis of clay minerals, randomly oriented powder specimens of the integral sample DU1–DU3 and MAR1 + MAR2 clay fractions were prepared and measured. The software SYBILLA (Chevron Inc., based on the algorithms of Drits and Sakharov, 1976) was employed to model the measured X-ray patterns of the textured specimens. During the modelling, the program continuously changes the content of the suggested phases to achieve the best fit between the model and the measured pattern, based

Table 1. Mass concentrations and sampling intervals during the SAMUM-1 winter campaign at Praia in 2008. Mass concentration values are given in μg per volumetric m^3 at 1013 hPa and 273.25 K. Sampling duration is given in hours and decimal fractions thereof. Sampling begin and end times are give as local time in the format YYYY-MM-DD hh:mm (ISO, 2004)

TSP			PM_{10} equivalent			$PM_{2.5}$ equivalent		
Begin of sampling	Duration (h)	$\mu g/m^3$	Begin of sampling	Duration (h)	$\mu g/m^3$	Begin of sampling	Duration (h)	$\mu g/m^3$
2008-01-13 14:47	25.03	90	2008-01-13 14:45	24.02	59	2008-01-13 14:42	24.07	18
2008-01-14 19:00	–	–	2008-01-14 15:39	20.08	42	2008-01-14 15:39	20.08	10
2008-01-15 16:41	16.90	67	2008-01-15 12:36	20.98	38	2008-01-15 12:37	20.97	17
2008-01-16 10:26	22.82	95	2008-01-16 10:46	22.58	40	2008-01-16 10:47	22.57	19
2008-01-17 10:41	23.82	228	2008-01-17 10:43	23.90	149	2008-01-17 10:51	23.32	67
2008-01-18 11:50	21.98	289	2008-01-18 11:54	22.05	189	2008-01-18 11:56	22.02	83
2008-01-19 10:49	22.70	318	2008-01-19 10:48	22.68	251	2008-01-19 10:47	23.00	93
2008-01-20 10:31	22.95	178	2008-01-20 11:14	22.22	137	2008-01-20 11:14	22.20	55
2008-01-21 10:18	23.05	158	2008-01-21 10:09	23.10	128	2008-01-21 10:09	23.12	49
2008-01-22 10:11	24.32	177	2008-01-22 10:01	24.48	148	2008-01-22 10:11	24.32	61
2008-01-23 11:15	22.12	148	2008-01-23 11:17	22.12	113	2008-01-23 11:18	22.08	47
2008-01-24 10:30	23.08	267	2008-01-24 10:30	23.08	251	2008-01-24 10:30	23.08	93
2008-01-25 10:06	23.43	235	2008-01-25 10:07	23.43	214	2008-01-25 10:06	23.45	72
2008-01-26 12:45	20.80	93	2008-01-26 12:43	20.82	71	–	–	–
2008-01-27 10:19	23.18	177	2008-01-27 10:19	23.17	120	2008-01-27 09:31	23.90	42
2008-01-28 10:22	22.82	525	2008-01-28 10:24	22.78	460	2008-01-28 10:23	22.87	181
2008-01-29 10:05	23.17	542	2008-01-29 10:06	23.15	460	2008-01-29 10:05	23.20	184
2008-01-30 10:57	22.47	342	2008-01-30 10:56	22.48	298	2008-01-30 10:58	22.45	102
2008-01-31 10:05	23.10	285	2008-01-31 10:05	23.10	183	2008-01-31 10:05	23.10	58
2008-02-01 09:47	23.60	356	2008-02-01 10:05	23.30	278	2008-02-01 10:06	23.28	114
2008-02-02 10:02	23.07	146	2008-02-02 10:02	23.07	200	2008-02-02 10:06	23.00	84
2008-02-03 09:36	23.78	81	2008-02-03 09:38	23.75	49	2008-02-03 09:42	23.65	23
2008-02-04 09:56	23.28	46	2008-02-04 09:57	23.28	26	2008-02-04 10:01	23.18	9
2008-02-05 09:45	23.57	46	2008-02-05 09:43	23.60	24	2008-02-05 09:49	23.50	8
2008-02-06 10:06	23.22	28	2008-02-06 10:07	23.20	17	2008-02-06 10:39	22.70	7
2008-02-07 09:48	23.88	39	2008-02-07 09:46	23.90	15	2008-02-07 09:57	23.72	5
2008-02-08 10:10	23.03	51	2008-02-08 10:09	23.05	15	2008-02-08 10:20	22.87	5
2008-02-09 09:37	23.58	35	2008-02-09 09:37	23.58	16	2008-02-09 09:53	23.33	6

Table 2. Specifications for measuring powder samples using (a) copper and (b) cobalt radiation and (c) for identifying clay minerals using textured specimens

	a	b	c
Manufacturer	Seifert	Seifert	Philips
Model	XRD 3003TT	XRD 3003TT	PW1050
Anode material	Cu K_α	Co K_α	Cu K_α
Angle (°2Θ)	3–70	3–70	5–50
Increment (°2Θ)	0.02	0.02	0.02
Time per step (s)	13	13	13
Tube voltage (kV)	40	50	40
Tube current (mA)	30	36	30

on the least squares method. As result, from the best-fit model the ratio of the clay phases in the sample can be estimated.

The aerosol size distributions in the submicron range were measured quasi-continuously by a combination of a Differential Mobility Particle Sizer (DMPS) for the mobility size range of 26–800 nm and an Aerodynamic Particle Sizer (APS; model 3321, TSI Inc., St. Paul, USA) for the aerodynamic size range of 570 nm to 10 μm, of which data only for particles smaller than 5 μm were used. For details of measurement and data processing refer to Schladitz et al. (2011). Particles in the size range of 4–500 μm were collected by a single-stage impactor (SSI) on glass substrates coated by silicon oil and a free-rotating wing impactor (FWI). For details of measurement and analysis refer to Kandler et al. (2009). A laboratory microscope (model BH2, Olympus GmbH, Hamburg, Germany) with a dedicated microscopy digital camera (ColorView I with analySIS 5 software, Olympus GmbH, Hamburg, Germany) was used for particle sizing and counting. Due to the constant magnification calibration with this new setup, the size error of the particles could be reduced to 3% for particles larger than 15 μm, and approximately 0.5 μm for smaller ones. The same corrections and image analysis procedures as described by Kandler et al. (2009) were applied. However, due to a higher degree of automation in terms of image acquisition, two full size distributions could be measured each day.

4. Results and Discussion

4.1. Meteorological situation

During the measurement campaign Cape Verde was under very stable atmospheric conditions. The wind direction was nearly always (>97% of the time) in the sector of 330° to 40° (NNW to NE) with a low variability (Fig. 2). The average wind direction was 11° and the average wind speed was 5.5 m/s during the campaign. According to aerosol mass concentration analysis and to the lidar investigation of the lowest accessible altitudes (Groß et al., 2011) as well as to the synoptic situation, the measurement campaign was split into three dust periods DU1, DU2 and DU3 and two maritime periods MAR1 and MAR2 (Knippertz et al., 2011). In terms of wind speed there was a difference between the dust and maritime periods (4.6 ± 1.5 m/s during dust condition, 7.1 ± 1.4 m/s during maritime ones), but no difference between the separate dust periods was found. Fig. 1 shows the dominant transport pathways derived from backward trajectory analysis for Praia (Knippertz et al., 2011) during the three dust events and three different trajectories from the maritime phases. In addition, source regions identified by the backward trajectory analysis in conjunction with satellite imagery and synoptic observations are shown (for details refer to Knippertz et al., 2011). While DU2 and DU3 are quite similar in terms of transport pattern and source region in the eastern Mali/western Niger area, during DU1 the dust was transported over a shorter distance from southern Mauritania. During the maritime phases MAR1 and MAR2, several transport pathways (examples shown in Fig. 1) occurred. The air masses on these paths were transported over the Atlantic Ocean for several days. However, if the backward trajectories for the marine boundary layer are calculated for 10 days (not shown), nearly all trajectories crossed the African continent, implying that all investigated airmasses were influenced continentally to some degree. This influence is confirmed by the measurements discussed in chapter 4.4 and the single particle chemical analysis presented by Kandler et al. (2011). For this reason, the term 'maritime' is used to denote these situations instead of 'marine', as practically no airmasses formed under pure marine influence were encountered in this work.

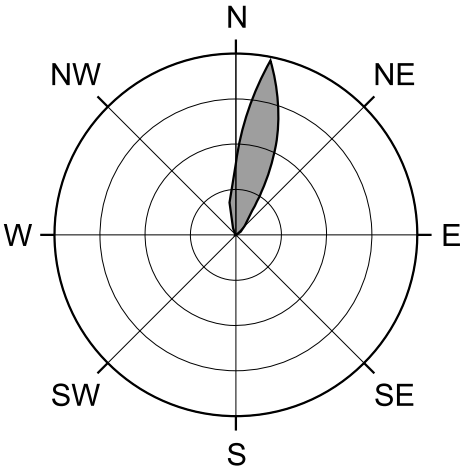

Fig. 2. Wind direction distribution at the Praia ground station during SAMUM-2.

From the temperature, relative humidity and atmospheric pressure the water vapour mixing ratio was calculated as a tracer for air mass and vertical mixing. Figure 3 shows time series of the water vapour mixing ratio and the deviation of wind direction from the average direction. In addition, the difference in water vapour mixing ratio between the daytime and nighttime values is shown as black bar. During the dust periods, a stronger diurnal pattern in water vapour mixing ratio (especially DU1 and DU3) and, less significant, in wind direction oscillation is present than during the maritime periods before and after the dust periods. This behaviour shows the influence of the dust burden on the local circulation around the island of Santiago. It indicates that in dust situations during daytime, when there is a decrease in

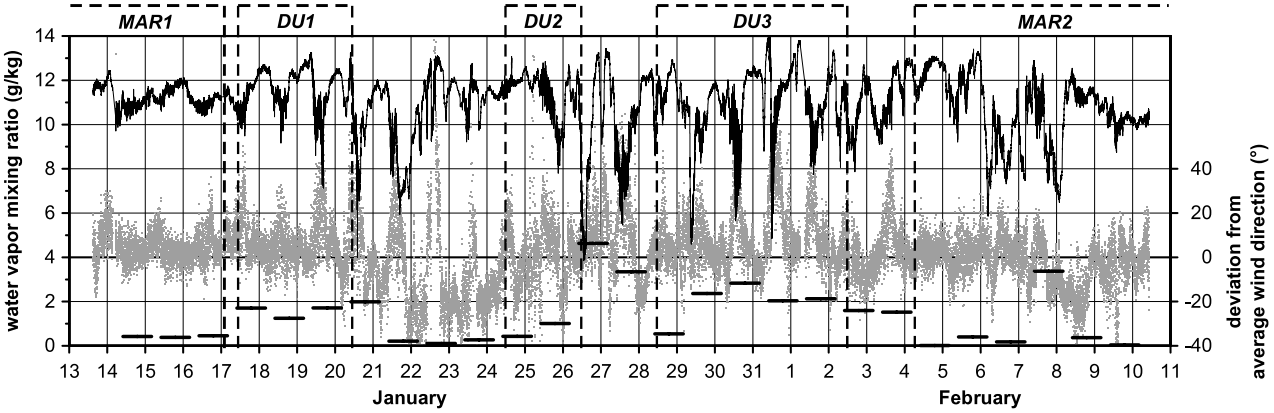

Fig. 3. Time series of water vapour mixing ratio (black line) and deviation from the average wind direction of 11° (grey dots). The short horizontal black lines in the lower half show the differences in mixing ratio between daytime (10–16 h) and nighttime (22 h to 4 h) averages. Dust (DU1, DU2, DU3) and maritime (MAR1, MAR2) periods are marked as identified by aerosol mass concentrations and lidar profiles.

water vapour mixing ratio, dry dust-laden air is mixed downward from the dust layer (Jaenicke and Schütz, 1978; Knippertz et al., 2011) into the local, more humid, marine boundary layer. That does not happen to the same extent during the maritime periods. In addition, a downmixing of momentum from the more easterly air flow in the dust layer into the more northerly flow of the marine boundary layer seems to occur, as the wind direction tends to the east during daytime in dust situations (Fig. 3). A similar behaviour of momentum downmixing has been reported for other locations (Banta and Cotton, 1981; McRae et al., 1981; Haeger-Eugensson, 1999).

4.2. *Mass concentration*

The aerosol mass concentrations at Praia appear as a superposition of advected mineral dust, small amounts of locally emitted dust and sea–salt (Kandler et al., 2011; see also Fig. 1 of Knippertz et al., 2011). During maritime situations, the average TSP mass concentration is 55 μg/m^3 while during dust advection it increases by a factor of 5 (275 μg/m^3). For the PM_{10}- and $PM_{2.5}$-equivalent mass concentrations, the increase is even higher (Fig. 4). The PM_{10} concentration of 29 μg/m^3 for the maritime period are similar to those found during summer time in 2006 at Cape Verde (Jeong et al., 2008), indicating a background mass concentration level with low variability. For dust periods, the PM_{10} concentration in 2008 of 223 μg/m^3 is considerably higher than these background concentrations. It is also higher than the concentrations reported for Sal island during a dust event (Westphal et al., 1988) and 2.5 times as high as the January average at Sal (Chiapello et al., 1995). Though there is a variation on day-to-day basis at Cape Verde of 43 to 52% relative standard deviation (Fig. 4), it has to be considered as a low variability in comparison to the values encountered during the SAMUM field experiment in Morocco (Kandler et al., 2009), where a relative standard deviation of 100–135% was measured for background situations and 135–180% during dust wind situations (all for daily averages). This difference indicates that the variability is smoothed out by the transport, either due to mostly removal of the highly variable ultra-large particle fraction (larger than 20 μm diameter) and/or due to a mixture of differently active sources. Daily mass concentrations are given in Table 1.

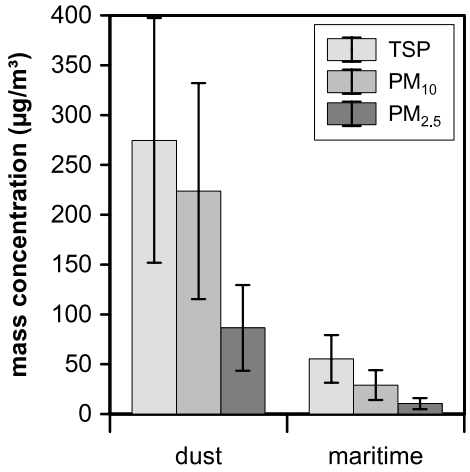

Fig. 4. Average mass concentrations and standard deviations for daily samples at Praia, Cape Verde; 'Dust' and 'Maritime' denote the average of the according periods.

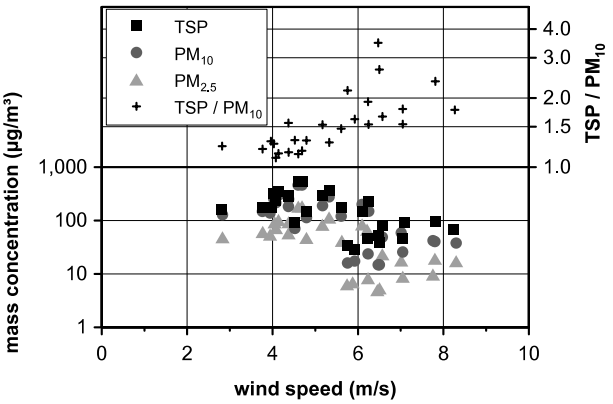

Fig. 5. Correlation of wind speed with mass concentrations (TSP, PM_{10}, $PM_{2.5}$; bottom panel) and ratio of TSP/PM_{10} (top panel).

Local dust production is usually increasing with increasing wind speed (Shao, 2008). While it was found in Morocco that the aerosol mass concentrations are strongly correlated with the wind speed (Kandler et al., 2009), indicating that a significant fraction of the mass concentration was produced locally, for Cape Verde the picture is different. We find a decreasing aerosol mass concentration with increasing wind speed (Fig. 5). In addition, no difference in strength of correlation for the different mass fractions is detected. This is also in contrast to Morocco, where—as it is to be expected for local dust production—the TSP mass concentration exhibited the strongest correlation with wind speed. The decrease of absolute mass concentration with increasing wind speed leads to two conclusions. First, the amount of locally influenced aerosol mass concentration is low, and secondly, the wind speed as determined by the meteorological situation shows lower values during dust transport. One possible explanation for the latter may be the hypothesis that radiation extinction of the dust leads to less energy input to the planetary surface and into the boundary layer and, thus, by reduced convection to a shallower boundary layer depth. With a decrease in convective activity and boundary layer depth the amount of momentum mixed down from the free atmospheric circulation above would also be decreased. However, this change in wind speed may also be related to the synoptic situation. Longer time series would be needed to assess this question.

In addition, Fig. 5 shows the dependency of the TSP/PM_{10} ratio on wind speed. While in Morocco much higher values

were encountered (low-dust situation: 8.6, dust-wind: 37), the TSP/PM_{10} ratio is comparatively low at Cape Verde, ranging from 1.24 (dust period average) to 2.44 (maritime period average). Notably, the ratio is higher for maritime situations than for dust transport. There are probably three concurrent explanations. Firstly, though the amount of locally produced dust is low at an absolute scale, it is present for the particles larger than 10 μm in aerodynamic diameter, especially when there is no advected dust and the local wind speeds are high. Secondly, with increasing wind speeds the effective settling velocity for particles between 20 and 50 μm diameter may decrease significantly (Noll and Fang, 1989; Aluko and Noll, 2006), so a higher fraction of larger particles may have been transported to Praia. Thirdly, a large amount of potentially deliquesced sea–salt—still deliquesced during the weighing process—may also lead to an increase of particle mass for particles with diameters greater than 10 μm (see also Schladitz et al., 2011). No conclusion on the prevailing process can be drawn from our data. The ratio $PM_{10}/PM_{2.5}$ of 2.67 is not influenced by the meteorological situation on Cape Verde, indicating a constant background aerosol situation, while in contrast the ratio of $PM_{10}/PM_{2.3}$ in Morocco increased from 3.4 during low-dust conditions to 5.1 during dust wind.

4.3. Aerosol size distribution

The knowledge of the full aerosol size distribution is crucial for the calculation of the radiative transfer. Figure 6 shows a compilation of the average size distributions during the campaign for the identified dust periods, for the maritime period, and the campaign average. In addition, the average size distribution for the SAMUM campaign in Morocco (Kandler et al., 2009) and for former campaigns on Cape Verde (Jaenicke et al., 1971; Jaenicke and Schütz, 1978) are shown. Finally, the volume size distributions for the averages of dust and maritime periods on Cape Verde are displayed. The size distributions can be well explained by a superposition of four log-normal distributions. The two modes with the smallest diameters can be interpreted as characteristic marine size distribution formed by sea–salt production and sulfate formation. However, the variability of the larger of the two modes in contrast to the smaller indicates an additional contribution of dust (see also Schladitz et al., 2011). The third mode with a modal value between 5 and 10 μm particle diameter can be clearly identified as mineral dust dominated mode by its chemical composition (Kandler et al., 2011) as well as wind speed measurements (see later). The forth mode is identified intermittently only by parameterization of the size distribution. Its modal diameter varies between 15 and 70 μm, and is interpreted as—at least in part—locally produced dust. Comparing the dust period size distributions in Fig. 6, it can be seen that during DU3 besides the mineral dust mode also the mode around 1 μm particle diameter is enhanced. This is in accordance with the results of electron microscopy (Kandler et al., 2011), which shows that an increased amount of small dust particles is present during DU3. Also, during the same period the fraction of hydrophobic particles is increased (Schladitz et al., 2011). In comparison to former size distribution measurements in the Cape Verde region (1969 and 1973), significantly higher dust loads were found in the dust mode during the 2008 campaign. Otherwise, the size distributions are quite similar to CV-1973 (see Fig. 6). Onboard the research vessel Meteor in 1969, lower concentrations were found for the size range with particle diameter greater than 10 μm, which may be related to an additionally local dust contribution for the largest particles during our campaign, which would not be expected for ship measurements. A large difference exists between the dust period size distributions on Cape Verde and the 'dust wind' size distribution in Morocco (Kandler et al., 2009), where three magnitudes higher concentrations of 100 μm diameter particle were present due to local production.

If the dust volume size distribution is calculated from the number size distribution (Fig. 6), an 'advected dust' volume size distribution can be determined as the positive difference between dust and maritime periods (Fig. 7). This advected volume size distribution is not necessarily valid for particles larger than 20 μm, as the higher wind speeds during the maritime periods may increase significantly the transport distances of these particles (Aluko and Noll, 2006), but it describes adequately the additional material for the smaller particles. The modal diameter of this advected dust is generally below 10 μm. The period DU1 has a slightly larger modal diameter than DU2 and DU3, which is in accordance with the shorter transport distances and times for this dust event. While the dust sources for Cape Verde during DU1 were located at the coast of Mauritania, they were located in the eastern Niger/western Mali region during DU2 and DU3. Notably, the general shape and intensity ratio of the two modes agree very well with those simulated for dust in the lower SAL in this region decades ago (Westphal et al., 1988, not shown in graph), while a higher overall concentration and smaller modal sizes were measured in 2008. Similar modal diameters of the larger mode between 6 and 10 μm in diameter were also found by high-volume filter sampling measurements onboard the research vessel Meteor in the Cape Verde region in 1998 (Stuut et al., 2005, shown as shaded area). In contrast, measurements farther to the northeast close to Cape Blanc (Stuut et al., 2005) as well as in the gulf of Guinea (Stuut et al., 2005, not shown) exhibit a considerably larger modal diameter. In conjunction with deep-sea sediment trap measurements confirming this difference (Ratmeyer et al., 1999b; Stuut et al., 2005) it can be concluded that the smaller modal diameters of the dust volume distribution encountered at Cape Verde are a persistent phenomenon, though Stuut et al. (2005) illustrated that it is not caused by a particular dust source.

In accordance with the mass concentration trends (fig. 1 of Knippertz et al., 2011), the average volume concentration during DU3 is approximately twice as high as that of the other periods.

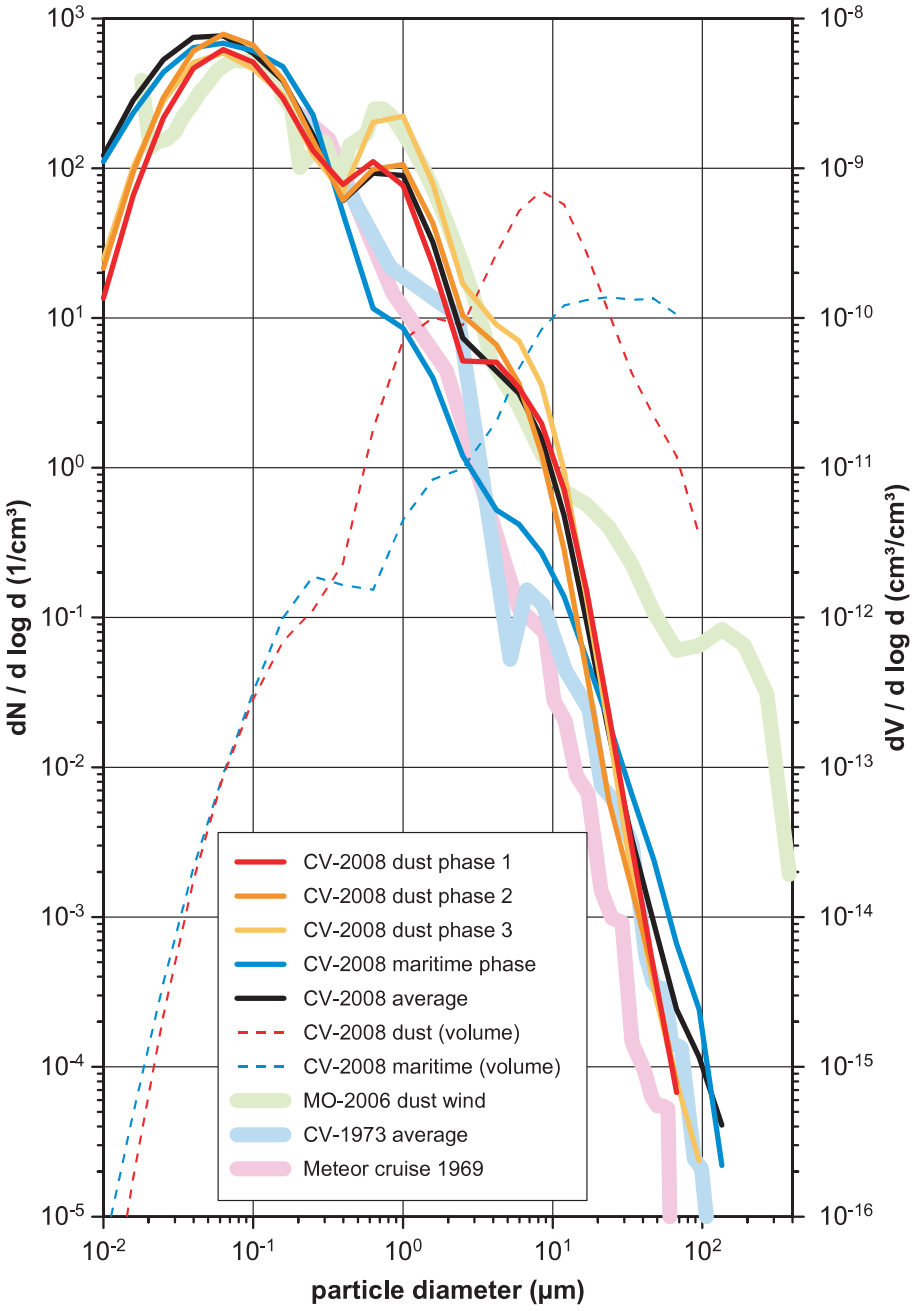

Fig. 6. Size distributions for meteorological periods during SAMUM-2 at Cape Verde (CV-2008), during SAMUM-1 in Morocco (MO-2006), from former campaigns at Cape Verde (CV-1973) and onboard the research vessel Meteor in the Cape Verde region in 1969.

While the uncertainties of the TSP mass measurements (increasing inlet losses with increasing particle size and, thus, mass contribution) do not allow a comparison with mass concentrations derived from the size distributions, a comparison of PM_{10} and $PM_{2.5}$ is possible, assuming a density of 1.5 g/cm^3 for particles with diameter smaller than 1 μm and 2.5 g/cm^3 for larger particles. This comparison leads to an excess in mass of 60% for the size distribution-derived PM_{10} values versus the ones measured by gravimetry, and to an excess of 30% for $PM_{2.5}$. Given the uncertainties in particle shape and density, which influence the comparison by affecting aerodynamic diameter and inlet losses, the agreement between the two methods is acceptable.

The averaged aerosol size distribution can be parameterized with a low error by three to four log-normal distributions. The parameters for the separate dust periods and the maritime period average as well as the campaign average are given in Table 3.

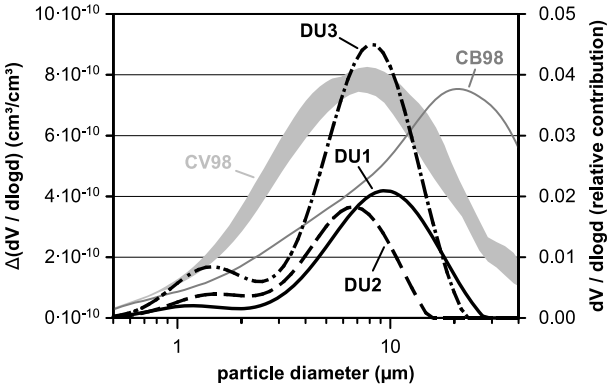

Fig. 7. 'Advected volume': difference of the single dust period volume size distributions and the maritime volume size distribution, each calculated from the according number size distributions (left axis). In addition, the volume size distribution range from previous measurements in the Cape Verde region (CV98) and near Cape Blanc, north-west Mauritania, (CB98) are shown (right axis, ship-borne measurements in 1998, Stuut et al., 2005).

Table 3. Parameters of the n-modal size distributions for the three dust periods, the maritime period and the average size distribution of the whole campaign

	i	n_i(cm^{-3})	m_i (μm)	ζ_i
Dust period 1	1	468.2	0.06942	2.018
	2	53.57	0.6901	1.594
	3	2.722	4.173	1.701
	4	5.878×10^{-4}	23.10	1.542
Dust period 2	1	610.9	0.06823	2.040
	2	53.90	0.8471	1.537
	3	3.792	3.356	1.647
	4	2.028×10^{-3}	16.53	1.652
Dust period 3	1	489.8	0.06485	2.104
	2	108.4	0.8612	1.513
	3	5.590	3.863	1.665
	4	3.244×10^{-4}	25.70	1.622
Maritime period	1	720.2	0.05756	2.306
	2	2.087	1.133	1.422
	3	0.6064	2.606	2.331
	4	9.125×10^{-5}	68.85	1.288
Average	1	741.3	0.05349	2.349
	2	43.50	0.8521	1.518
	3	2.779	3.768	1.704
	4	4.009×10^{-3}	14.74	1.801

Aerosol size distribution as a function of the particle diameter d_p can be calculated as

$$\frac{dn}{d\ \log\ d_p} = \frac{\ln 10}{\sqrt{2\pi}} \sum_{i=1}^{4} \frac{n_i}{\ln\zeta_i} \exp\left(-\frac{\ln^2\left(d_p m_i^{-1}\right)}{2\ln^2\zeta_i}\right) \quad (1)$$

with n_i, m_i, ζ_i the parameters of the log-normal distributions.

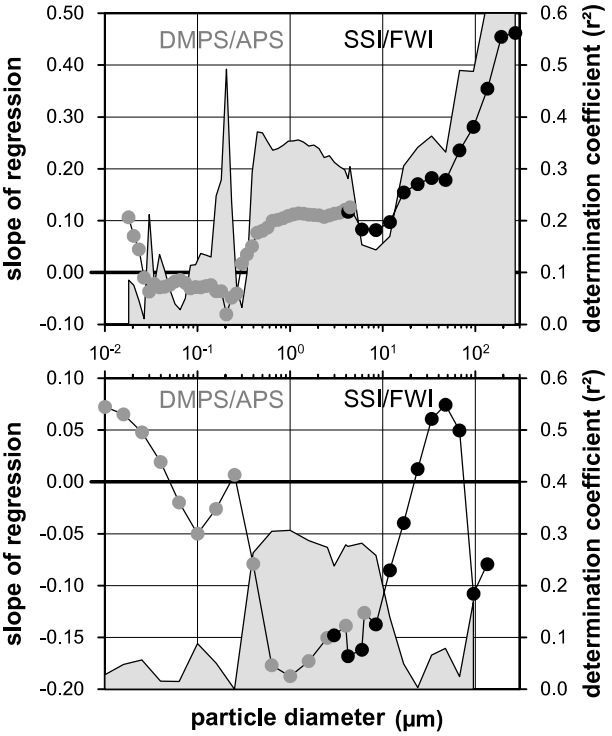

Fig. 8. Size distributions of the correlation between particle number concentrations derived by different methods (grey symbols: DMPS and APS, black symbols: SSI and FWI) with wind speed for Morocco (top panel) and Cape Verde (bottom panel); the determination coefficient (square of the correlation coefficient) is drawn as shaded area.

To assess a potential connection between dust concentration and local meteorology, the time series of all particle concentrations for each particle size interval were correlated with the wind speed. Figure 8 shows the size dependence of the regression coefficient and the according determination coefficient for these correlations. For the SAMUM Morocco campaign in 2006, there is no correlation between wind speed and concentration for particles smaller than 400 nm. Between 400 nm and 10 μm in particle diameter, there is a constantly positive regression coefficient showing a correlation with wind speed. The regression coefficient increases strongly with particle size for particles larger than 10 μm. This shows that in Morocco the local wind speed is the controlling factor for the particle concentrations of the large particles. At Cape Verde, again there is no correlation for particles smaller than 400 nm. However, for particles between 400 nm and 15 μm in particle diameter, there is an anti-correlation between particle concentration and wind speed, for which possible causes were explained in this chapter earlier. For even larger particles there is a (very weak) positive correlation again. A similar behaviour of the correlation between particle number concentrations and local wind speed has been described for Sal, Cape Verde (Jaenicke and Schütz, 1978). From this statistical approach and the 'advected dust volume' distributions, we can

conclude with confidence that the local influence during dust advection to the Cape Verde islands the aerosol in the size range between 400 nm and 20 μm is negligible.

4.4. Mineralogical composition

All TSP filter samples yielded appropriate XRD intensities for mineral identification as well as for quantitative phase determination using the RIR method. The aerosol is composed of varying abundances of quartz, potassium feldspar, plagioclase, magnesium-rich calcite, gypsum, halite, rutile and clay mineral phases. The latter ones consist of mineral members from the kaoline, illite and chlorite group as well as smectite. Measurements with cobalt radiation showed no goethite, hematite or magnetite (experimentally determined identification limit $\approx 1\%$). However in the textured specimens, where the Fe-phases are enriched due to their small grain sizes, discrete amounts of goethite could be detected. We believe that its formation reflects a hydrolysis of hematite/magnetite or the iron was leached out from existing silicates.

Diffraction patterns for the textured samples are shown in Fig. 9, following the suggestion of Środoń and Eberl (1980). In addition, raw diffraction data are available as appendix in the electronic supporting information. An overview of the semi-quantitative results for the individual samples is given in Table 4 (diffraction patterns are shown in Fig. 10). Kaoline is the dominant mineral during the all the periods, whilst illite is also present along the entire period of measurements (minimum content of 5%wt., Carroll, 1970). A disordered smectite component is present in most of the samples, which is evidenced by the asymmetrical shape of basal illite 001 peaks ($\sim$8.83 °2Θ) in the XRD patterns of textured specimens, as well as by the pronounced bulging in the 25 to 35 °2Θ area (Fig. 9). In some of the daily powder samples (DU3: Jan 28 to Feb 2, Table 4 and Fig. 10) the 001 reflections of the swelling phases are detected. The sharp and relatively intense reflections near 17.7 °2Θ are due to the superposition of the smectite 003 and illite 002 reflections, typical for ordered mixed layers (illite 1M—smectite of rectorite type), which is corroborated by the lack of the clear peak pattern of the air-dried illite 001 10Å lines. The described characteristics suggest a smectite content of 15–25% in illite, as well as the 1M illite polytype, implying the origin via in-place alteration of silicate phases (e.g. feldspar, biotite). Although the XRD patterns suggest a dominance of ordered kaolinite, a low amount of kaolinite/smectite mixed layers is also present, shown by the unusual basal asymmetry and broadening at the 001 reflections (12.37 °2Θ, Fig. 9). This implies that the smectite content in kaolinite is larger than 5%. Chlorite was detected only sporadically in daily powder samples in the DU3 period (Jan 27 to Feb 2, Table 4 and Fig. 10). A clay phase composition modelling—performed in the SYBILLA program—for the textured samples confirmed kaolinite as dominant clay mineral phase ($\sim$50–70%), with a considerable amount of smectite and illite components (approximately 10–15% and about 25–35%, respectively). Hence, the illite/kaolinite ratio is determined to be within the range from approximately 1 : 2 (DU1 period) to 1 : 4 (DU3 period).

The gravimetrically determined clay contents ranged between 30 and 60%wt. (Table 4). The maximum abundances of clay phases is found during the DU3 period. During the periods MAR1 and MAR2 periods, a comparatively lower amount of clay minerals is present. Since the mineral composition of DU1, DU2 and DU3 did not vary considerably, the mean concentration of the dust periods was calculated. The results were compared

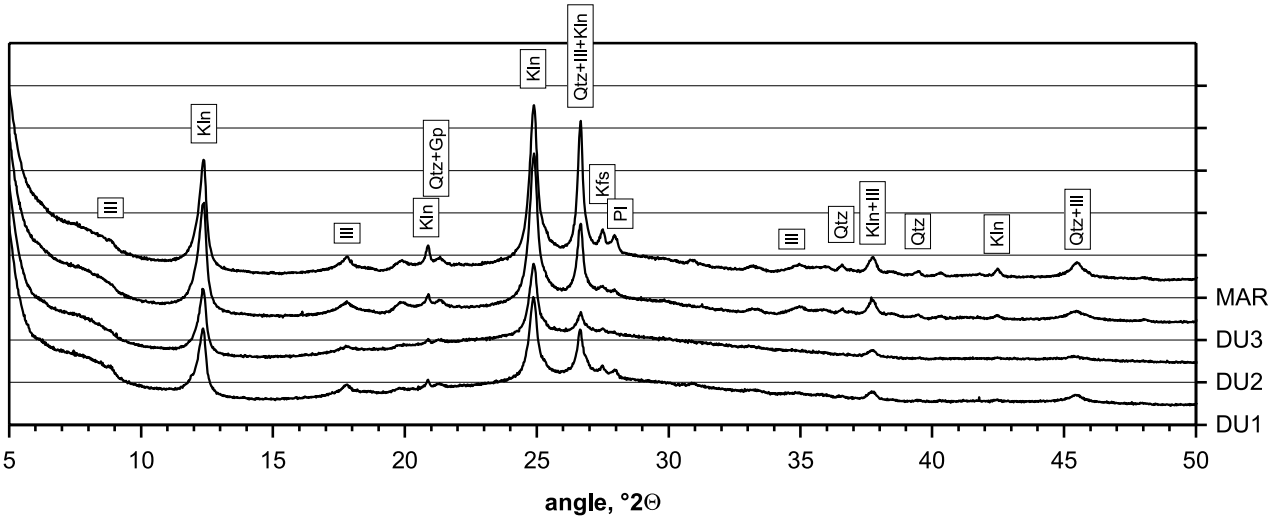

Fig. 9. Diffractograms of the textured sum samples for the three dust periods and the maritime period. Each major division on the *y*-axis equals 5000 counts. The curves and the according zero base lines are identified on the right of the graph. Major peaks are identified: Ill, illite; Kln, kaolinite; Qtz, quartz; Kfs, K-feldspar; Pl, plagioclase; Gp, gypsum (Kretz, 1983).

Table 4. Mineralogical composition of the TSP filter samples at Praia in 2008; a semiquantification is indicated by symbols: not detected (–), detected (+), traces (*), minor compound (**), major compound (***), dominant compound (****); the clay fraction column lists the mass fraction of insoluble particles smaller than 2 μm in the sample; the last column shows meteorological periods of dust (DU1, DU2, DU3) and maritime (MAR1, MAR2) influence and transitional periods (T); [1] and [2]: two samples were taken on this day; Qtz, quartz; Pl, plagioclase; Kfs, K-feldspar; Cal, calcite; Gp, gypsum; Hl, Halite; Ill, illite; Kln, kaolinite; Sme, smectite (swelling phase); Chl, chlorite; Rt, rutile (mineral abbreviations after Kretz, 1983).

Date	Qtz	Pl	Kfs	Cal	Gp	Hl	Ill (1M)	Kln	Sme	Chl	Rt	Clay fraction	Period
Jan 14	***	*	**	*	***	***	*	**	+	–	–	0.16	MAR1
Jan 15	***	+	**	*	**	***	*	*	+	–	–	0.25	MAR1
Jan 16[1]	*	*	**	–	*	**	+	*	+	–	**	0.51	MAR1
Jan 16[2]	***	–	*	*	**	***	+	**	+	–	–	0.23	MAR1
Jan 17	****	**	***	*	*	**	*	***	+	–	–	0.53	DU1
Jan 18	****	**	***	*	*	**	*	***	+	–	–	0.43	DU1
Jan 19	****	**	***	*	**	*	*	***	–	–	–	0.42	DU1
Jan 20	***	**	***	*	**	*	*	***	–	–	–	0.68	DU1
Jan 21	***	**	**	*	*	*	*	***	+	–	–	0.53	T
Jan 22	***	**	**	*	**	*	*	***	+	–	–	0.40	T
Jan 23	***	*	**	*	*	**	*	***	+	–	–	0.57	DU2
Jan 24	***	***	***	*	*	*	*	***	+	–	–	0.68	DU2
Jan 25	***	***	**	*	*	*	*	****	*	+	–	0.66	DU2
Jan 26	***	*	**	*	*	**	*	***	+	–	–	0.56	T
Jan 27	**	**	**	*	*	*	*	***	+	+	–	0.45	T
Jan 28	***	**	**	*	*	*	*	***	*	+	–	0.56	DU3
Jan 29	**	**	***	*	*	*	*	***	*	+	–	0.60	DU3
Jan 30	***	**	**	*	*	*	*	***	*	+	–	0.47	DU3
Jan 31	***	**	**	*	*	*	*	***	*	+	–	0.49	DU3
Feb 01	***	**	***	*	*	*	*	***	*	+	–	0.56	DU3
Feb 02	**	**	**	*	*	**	*	***	*	+	–	0.58	T
Feb 03	**	**	**	*	**	**	*	**	–	–	*	0.43	T
Feb 04	***	**	***	–	***	**	*	*	–	–	+	0.17	MAR2
Feb 05	**	+	**	*	*	**	–	*	+	–	–	0.26	MAR2
Feb 06	**	–	**	*	*	**	+	**	+	–	–	0.30	MAR2
Feb 07	***	*	**	*	**	***	–	**	–	–	–	0.23	MAR2
Feb 08	**	+	*	*	*	**	*	**	–	–	–	0.61	MAR2
Feb 09	*	–	*	–	–	***	–	*	–	–	–	0.55	MAR2

with the mineral abundances of MAR1 and MAR2 (Fig. 11). During the dust periods, kaolinite, potassium feldspar, quartz and illite/smectite dominated the dust composition. Plagioclase, calcite, gypsum and halite were minor constituents. Quartz, strongly weathering-resistant due to its high mechanical and chemical stability, can be found in similar quantities during the MAR periods as well. The concentration of kaolinite, although still the dominant mineral, decreases during the MAR periods with low Saharan dust contribution (Knippertz et al., 2011). In contrast, potassium feldspar concentrations are increased, indicating a possible minor contribution of local soil material. Halite and gypsum occur at significantly higher concentrations during the MAR periods, similar to prior observations at the Canary Islands (Alastuey et al., 2005). While halite is most probably directly emitted by sea spray, gypsum is only partly of marine origin (Hoornaert et al., 1996) and may also be processed calcite (e.g. Glaccum and Prospero, 1980). During the MAR periods on several occasions (Jan 16, Feb 3 and Feb 4) a rutile presence was measured. Between the dust phases only weak differences are visible. At the beginning of DU1 there is a higher contribution of quartz to the aerosol (Table 4), which is probably connected the slightly higher abundance of particles around 10 μm diameter (Fig. 7), being probably related to the shorter transport pathway and/or to the different source region of DU1. Small amounts of chlorite are measured only during DU3. However, at this point it can't be determined whether this detection is due to a different aerosol composition during DU3 or due to a lower relative detection limit caused by the highest aerosol mass concentrations during this phase.

In comparison to the SAMUM-1 campaign (Kandler et al., 2009), the most pronounced difference occurs in the mean abundance of clay and non-clay minerals. At Cape Verde, significantly higher concentration of clay minerals occur, most probably due to the higher settling velocities of the larger non-clay

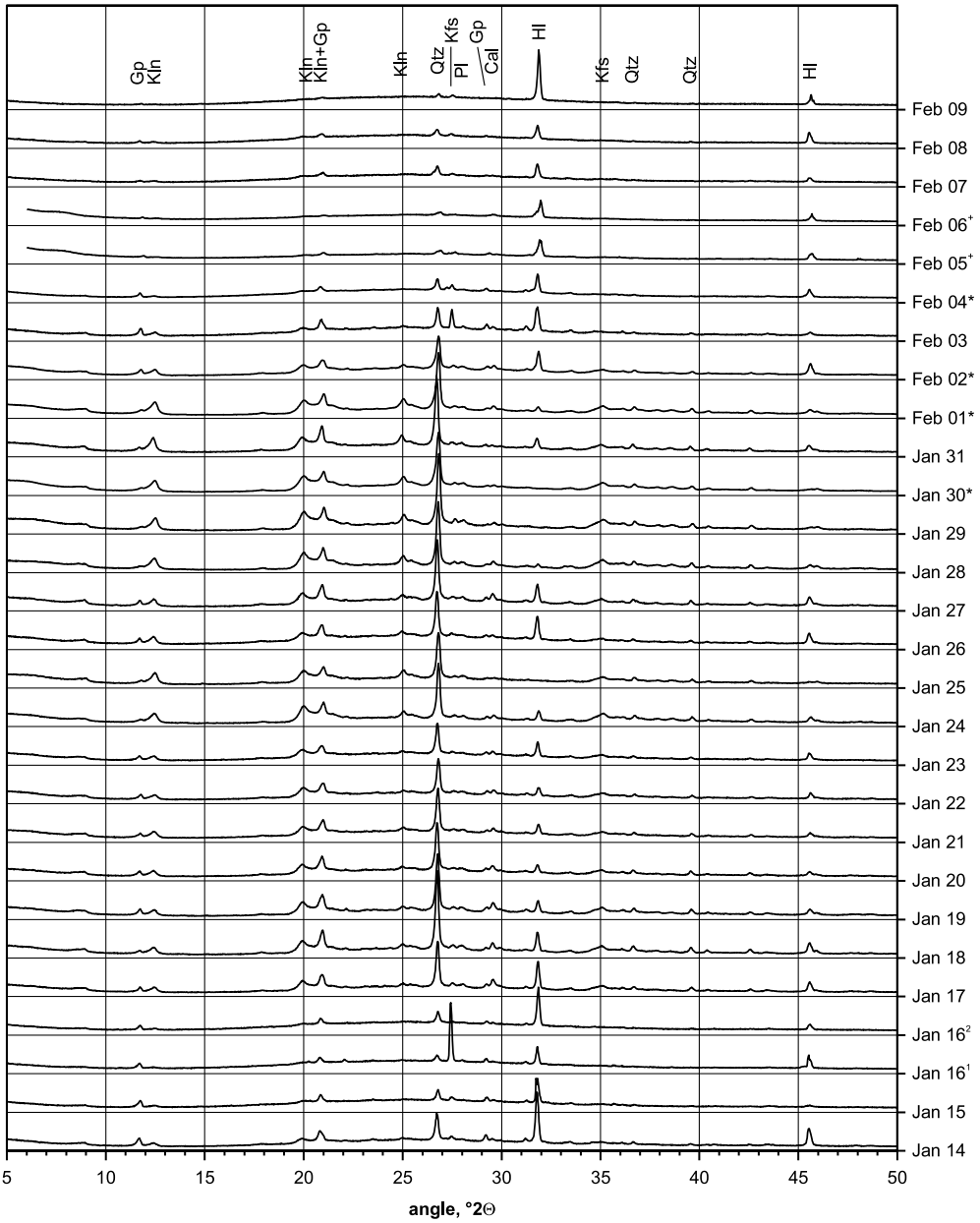

Fig. 10. Diffractograms of the TSP powder samples at Praia. Each division on the *y*-axis equals 10000 counts. The curves and the according zero base lines are identified on the right of the graph. $^{+}$, samples were measured with Philips instrument (see Table 2); *, count rates were scaled by 0.2 to match the standard instrument settings; ^{1} and ^{2}, two samples were collected on this day. Major peaks in the spectra are identified: Gp, gypsum; Kln, kaolinite; Qtz, quartz; Kfs, K-feldspar; Pl, plagioclase; Cal, calcite; Hl, halite (Kretz, 1983).

particles in comparison to the smaller and platy clay minerals and the subsequent loss of the former during transport. A similar behaviour concerning the clay mineral content is reported by Formenti et al. (2008) who measured mineral dust over western Africa.

During the total SAMUM-2 campaign described in this work, a dominance of kaolinite was found for the clay minerals. This is in accordance with the works of Caquineau et al. (1998, 2002), who detected high values of kaolinite at Sal Island, Cape Verde. These high values were found especially for air mass trajectories indicating Sahelian, south and central Saharan origin—meteorological situations similar to those encountered during the SAMUM-2 field campaign (Knippertz et al., 2011). The increase of kaolinite towards the equator is also shown by Chester et al. (1972) and Stuut et al. (2005). Kaolinite dominance was confirmed over Mali—a preferential source region

for this campaign—by Kiefert et al. (1996). In contrast to these findings, Glaccum and Prospero (1980) reported that the aerosol bulk mineralogy at Cape Verde Islands is dominated by illite. As higher illite than kaolinite concentrations are reported usually for other regions like the Canary Islands (Kandler et al., 2007), Israel (Falkovich et al., 2001), Sardinia (Guerzoni et al., 1997), northeastern Spain (Avila et al., 1997) and over the North Atlantic Ocean west of the African coast (Chester et al., 1971; Chester and Johnson, 1971; Chester et al., 1972), the measurements of Glaccum and Prospero (1980) have to be treated as unique.

5. Summary and Conclusions

During the SAMUM-2 campaign in January and February 2008 at Cape Verde, three major dust events were recorded. At the beginning and the end of the field campaign rather maritime conditions were encountered. During the dust events, the total mass concentration is raised by a factor of more than 10 over the maritime mass concentration, demonstrating the strong impact of Saharan dust advection on the aerosol load at Cape Verde. In general, the dust events can also be clearly distinguished from maritime periods by changing diurnal patterns in water vapour mixing ratio and wind direction. The wind speed is usually lower and the diurnal pattern in mixing ratio is less pronounced during dust advection compared to maritime conditions, indicating a lower input of energy to the boundary layer and a decoupling from the air layers above.

The size distribution measurements show number maxima around 50 to 70 nm particle diameter. Four modes can be identified in the spectra, of which the smallest belongs to sea-generated and sulfate aerosol. From the variability of the second mode around 700 nm particle diameter it can be concluded that it is a superposition of marine aerosol and advected mineral dust. The third mode between 5 and 10 μm can be attributed to sea–salt and dust in changing proportions. The fourth mode with modal sizes larger than 10 μm is attributed to mineral dust only (Kandler et al., 2011). The main size region of dust transported to the Cape Verde lies between 400 nm and 20 μm in particle diameter. For the first dust period DU1, where the most probable source areas were located closer than for the other periods, a slightly higher mass concentration was found to be associated with larger particles, reflected also by the size distribution measurements showing a slightly higher abundance of larger particles around 10 μm diameter. In addition, a higher relative quartz abundance is found during this phase. These observations can be explained by the shorter transport distance and, subsequently, less sedimentation losses during transport. In general, the dust concentrations encountered in 2008 were higher than those of earlier measurements at Cape Verde (Westphal et al., 1988; Jeong et al., 2008), but of course much lower than those encountered close to the sources (Kandler et al., 2009). For the largest particles there was a small local contribution, which was mainly detectable during maritime situations, similar to previous observations (Jaenicke and Schütz, 1978).

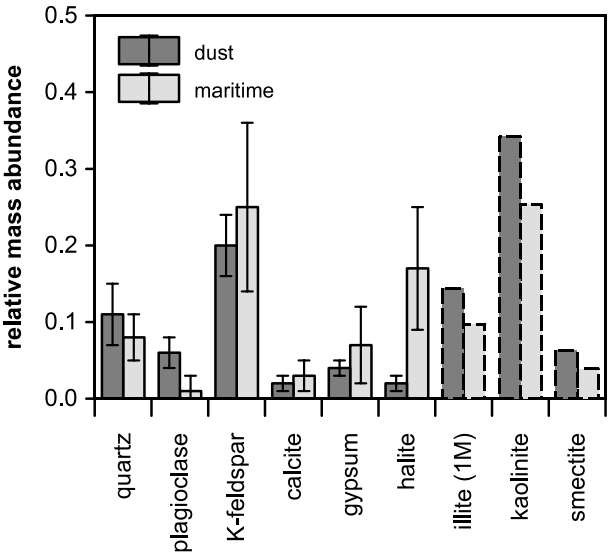

Fig. 11. Average mineralogical composition of TSP filter samples for the dust periods and for the maritime period at Praia, Cape Verde, given in mass fraction. The error bars from quartz to halite represent the standard deviation (1σ) of the measured daily samples; the clay mineral contents were estimated by multiplying the relative clay mineral ratios determined from the textured samples (see text for details) with the mass fraction of grains smaller than 2 μm diameter.

The mineralogical composition revealed kaolinite as the dominating clay mineral. In comparison with measurements in Morocco (Kandler et al., 2009), this clearly reflects the difference in source regions for both locations (Caquineau et al., 1998; Formenti et al., 2010). The mineralogical measurements also confirmed that the aerosol during the three dust periods was composed—within experimental errors—of the same components. In comparison to Morocco, a significantly higher amount of clay minerals was identified in the aerosol, reflecting the preferential removal of the large particles, which are to a higher extent composed of non-clay minerals (Kandler et al., 2009). A large difference in mineralogical composition was found between the dust and the maritime periods. During the latter, a significant amount of halite and gypsum was detected in the aerosol. Lower amounts of plagioclase and slightly higher amounts of K-feldspar during the maritime situations may indicate a change in particle source and may be a local contribution. However, also during the maritime periods the mineral dust has a significant and mostly dominating contribution to the aerosol mass at Cape Verde.

Acknowledgment

This study was supported by the German Research Foundation (DFG contract FOR 539) in the framework of the research group SAMUM. We thank especially TACV—Cabo Verde Airlines

and Mr. António Lima Fortes for great logistic support. We are grateful for the extraordinary preparation of the equipment provided by Berthold Friederich, Christian von Glahn and by the workshops of the IPA, Mainz. We thank the anonymous reviewer and Jan-Berend Stuut for their helpful and constructive comments.

References

Alastuey, A., Querol, X., Castillo, S., Escudero, M., Avila, A. and co-authors. 2005. Characterisation of TSP and PM2.5 at Izaña and Sta. Cruz de Tenerife (Canary Islands, Spain) during a Saharan Dust Episode (July 2002). *Atmos. Environ.* **39**, 4715–4728.

Aluko, O. and Noll, K. E. 2006. Deposition and suspension of large, airborne particles. *Aerosol Sci. Technol.* **40**, 503–513.

Andreae, M. O. and Rosenfeld, D. 2008. Aerosol–cloud–precipitation interactions. Part 1. The nature and sources of cloud-active aerosols. *Earth-Sci. Rev.* **89**, 13–41.

Ansmann, A., Baars, H., Tesche, M., Müller, D., Althausen, D. and co-authors. 2009. Dust and smoke transport from Africa to South America: lidar profiling over Cape Verde and the Amazon rainforest. *Geophys. Res. Lett.* **36**, L11802, doi:10.1029/2009GL037923.

Ansmann, A., Petzold, A., Kandler, K., Tegen, I., Wendisch, M. and co-authors. 2011. Saharan Mineral Dust Experiments SAMUM-1 and SAMUM-2: what have we learned? *Tellus* **63B**, this issue.

Avila, A., Queralt-Mitjans, I. and Alarcón, M. 1997. Mineralogical composition of African dust delivered by red rains over northeastern Spain. *J. Geophys. Res.* **102**, 21977–21996.

Banta, R. and Cotton, W. R. 1981. An analysis of the structure of local wind systems in a broad Mountain Basin. *J. Appl. Meteorol.* **20**, 1255–1266.

Biscaye, P. E., Chesselet, R. and Prospero, J. M. 1974. Rb-Sr, $^{87}Sr/^{86}Sr$ isotope system as an index of provenance of continental dusts in the open Atlantic Ocean. *J. Rech. Atmos.* **8**, 819–829.

Brindley, G. W. 1980. Quantitative X-ray mineral analysis of clays. In: *Crystal Structures of Clay Minerals and their X-Ray Identification* (eds. G. W. Brindley and G. Brown). Mineralogical Society, London, 411–438.

Caquineau, S., Gaudichet, A., Gomes, L. and Legrand, M. 2002. Mineralogy of Saharan dust transported over northwestern tropical Atlantic Ocean in relation to source regions. *J. Geophys. Res.* **107**, 4251, doi:10.1029/2000JD000247.

Caquineau, S., Gaudichet, A., Gomes, L., Magonthier, M.-C. and Chatenet, B. 1998. Saharan dust: clay ratio as a relevant tracer to assess the origin of soil-derived aerosols. *Geophys. Res. Lett.* **25**, 983–986.

Carlson, T. N. and Benjamin, S. G. 1980. Radiative heating rates for Saharan dust. *J. Atmos. Sci.* **37**, 193–213.

Carlson, T. N. and Prospero, J. M. 1972. The large-scale movement of Saharan air outbreaks over the northern equatorial Atlantic. *J. Appl. Meteorol.* **11**, 283–297.

Carroll, D. 1970. *Clay Minerals: A Guide to Their X-Ray Identification*. Geological Society of America, Boulder, Colorado.

Chen, G., Ziemba, L. D., Chu, D. A., Thornhill, K. L., Schuster, G. L. and co-authors. 2011. Observations of Saharan dust microphysical and optical properties from the Eastern Atlantic during NAMMA airborne field campaign. *Atmos. Chem. Phys.* **11**, 723–740.

Chester, R., Elderfield, H. and Griffin, J. J. 1971. Dust transported in the North-east and South-east Trade Winds in the Atalntic Ocean. *Nature* **233**, 474–476.

Chester, R., Elderfield, H., Griffin, J. J., Johnson, L. R. and Padgham, R. C. 1972. Eolian dust along the eastern margins of the Atlantic Ocean. *Mar. Geol.* **13**, 91–105.

Chester, R. and Johnson, L. R. 1971. Atmospheric Dusts collected off the West African Coast. *Nature* **229**, 105–107.

Chiapello, I., Bergametti, G., Gomes, L., Chatenet, B., Dulac, F. and co-authors. 1995. An additional low layer transport of Sahelian and Saharan dust over the North-Eastern Tropical Atlantic. *Geophys. Res. Lett.* **22**, 3191–3194.

Chiapello, I., Moulin, C. and Prospero, J. M. 2005. Understanding the long-term variability of African dust transport across the Atlantic as recorded in both Barbados surface concentrations and large-scale Total Ozone Mapping Spectrometer (TOMS) optical thickness. *J. Geophys. Res.* **110**, D18S10, doi:10.1029/2004JD005132.

Chipera, S. J. and Bish, D. L. 2002. FULLPAT: a full-pattern quantitative analysis program for X-ray powder diffraction using measured and calculated patterns. *J. Appl. Crystallogr.* **35**, 744–749.

Chung, F. H. 1974. Quantitative interpretation of X-ray diffraction patterns of mixtures. I. Matrix-flushing method for quantitative multicomponent analysis. *J. Appl. Crystallogr.* **7**, 519–525.

Darwin, C. 1846. An account of the fine dust which often falls on vessels in the Atlantic Ocean. *Quart. J. Geol. Soc. London* **2**, 26–30.

DeMott, P., Sassen, K., Poellot, M., Baumgardner, D., Rogers, D. and co-authors. 2003. African dust aerosols as atmospheric ice nuclei. *Geophys. Res. Lett.* **30**, 1732, doi:10.1029/2003GL017410.

Drits, V. A. and Sakharov, B. A. 1976. *X-ray Analysis of Mixed-layer Minerals*. Nauka (in Russian), Moscow.

Falkovich, A. H., Ganor, E., Levin, Z., Formenti, P. and Rudich, Y. 2001. Chemical and mineralogical analysis of individual mineral dust particles. *J. Geophys. Res.* **106**, 18029–18036.

Formenti, P., Andreae, M. O., Lange, L., Roberts, G., Cafmeyer, J. and co-authors. 2001. Saharan dust in Brazil and Suriname during the Large-Scale Biosphere-Atmosphere Expermient in Amazonia (LBA)-Cooperative LBA Airborne Regional Experiment (CLAIRE) in March 1998. *J. Geophys. Res.* **106**, 14919–14934.

Formenti, P., Rajot, J. L., Desboeufs, K., Caquineau, S., Chevaillier, S. and co-authors. 2008. Regional variability of the composition of mineral dust from western Africa: results from the AMMA SOP0/DABEX and DODO field campaigns. *J. Geophys. Res.* **113**, D00C13, doi:10.1029/2008JD009903.

Formenti, P., Schütz, L., Balkanski, Y., Desboeufs, K., Ebert, M. and co-authors. 2010. Recent progress in understanding physical and chemical properties of mineral dust. *Atmos. Chem. Phys. Discuss.* **10**, 31187–31251.

Glaccum, R. A. and Prospero, J. M. 1980. Saharan aerosols over the tropical north Atlantic – Mineralogy. *Mar. Geol.* **37**, 295–321.

Groß, S., Gasteiger, J., Freudenthaler, V., Wiegner, M., Geiß, A. and co-authors. 2011. Characterization of the planetary boundary layer during SAMUM-2 by means of lidar measurements. *Tellus* **63B**, this issue.

Grousset, F., Biscaye, P. E., Zindler, A., Prospero, J. and Chester, R. 1988. Neodymium isotopes as tracers in marine sediments and aerosols: North Atlantic. *Earth Planet. Sci. Lett.* **87**, 367–378.

Grousset, F., Rognon, P., Coudé-Gaussen, G. and Pedemay, P. 1992. Origins of peri-Saharan dust deposits traced by their Nd and Sr isotopic composition. *Paleogeog. Paeloclim. Paleoecol.* **93**, 201–212.

Guerzoni, S., Molinaroli, E. and Chester, R. 1997. Saharan dust inputs to the western Mediterranean Sea: depositional patterns, geochemistry and sedimentological implications. *Deep-Sea Res. II* **44**, 631–654.

Haeger-Eugensson, M. 1999. Vertical Interactions in a Nocturnal Multi-Scale Wind System Influenced by Atmospheric Stability in a Coastal Area. *Theor. Appl. Climatol.* **64**, 69–82.

Heintzenberg, J. 2009. The SAMUM-1 experiment over Southern Morocco: overview and introduction. *Tellus* **61B**, 2–11.

Hoornaert, S., Van Malderen, H. and Van Grieken, R. 1996. Gypsum and other calcium-rich aerosol particles above the North Sea. *Environ. Sci. Technol.* **30**, 1515–1520.

Huang, J., Zhang, C. and Prospero, J. M. 2010. Africa dust outbreaks: a satellite perspective of temporal and spatial variability over the tropical Atlantic Ocean. *J. Geophys. Res.* **115**, D05202, doi:10.1029/2009JD012516.

ICDD 2002. *Powder Diffraction File PDF-2*. JCPDS – International Center for Diffraction Data, Newton Square, PA, USA.

ISO 2004. Data elements and interchange formats—Information interchange—Representation of dates and times. In: *ISO 8601:2004*. ISO, Geneva, Switzerland, 33.

Jaenicke, R., Junge, C. and Kanter, H. J. 1971. Measurements of the aerosol size distribution over the Atlantic ocean. *Meteorol. Forschungsergeb. B* **7**, 1–54.

Jaenicke, R. and Schütz, L. 1978. Comprehensive study of physical and chemical properties of the surface Aerosols in the Cape Verde Islands Region. *J. Geophys. Res.* **83**, 3585–3599.

Jeong, G.-R. and Sokolik, I. N. 2007. Effect of mineral dust aerosols on the photolysis rates in the clean and polluted marine environments. *J. Geophys. Res.* **112**, D21308, doi:10.1029/2007JD008442.

Jeong, M.-J., Tsay, S.-C., Ji, Q., Hsu, N. C., Hansell, R. A. and co-authors. 2008. Ground-based measurements of airborne Saharan dust in marine environment during the NAMMA field experiment. *Geophys. Res. Lett.* **35**, L20805, doi:10.1029/2008GL035587.

Jickells, T. D., An, Z. S., Andersen, K. K., Baker, A. R., Bergametti, G. and co-authors. 2005. Global iron connection between desert dust, ocean biogeochemistry, and climate. *Science* **308**, 67–71.

Junge, C. 1979. The importance of mineral dust as an atmospheric constitutent. In: *Scope 14: Saharan Dust – Mobilisation, Transport, Deposition* (ed. C. Morales). John Wiley & Sons, Chichester, 49–60.

Junge, C. and Jaenicke, R. 1971. New results in background aerosols studies from the Atlantic expedition of the R. V. Meteor, spring 1969. *J. Aerosol Sci.* **2**, 305–314.

Kandler, K., Benker, N., Bundke, U., Cuevas, E., Ebert, M. and co-authors. 2007. Chemical composition and complex refractive index of Saharan Mineral Dust at Izaña, Tenerife (Spain) derived by electron microscopy. *Atmos. Environ.* **41**, 8058–8074.

Kandler, K., Lieke, K., Benker, N., Emmel, C., Küpper, M. and co-authors. 2011. Electron microscopy of particles collected at Praia, Cape Verde, during the Saharan Mineral dust experiment: particle chemistry, shape, mixing state and complex refractive index. *Tellus* **63B**, this issue.

Kandler, K., Schütz, L., Deutscher, C., Hofmann, H., Jäckel, S. and co-authors. 2009. Size distribution, mass concentration, chemical and mineralogical composition, and derived optical parameters of the boundary layer aerosol at Tinfou, Morocco, during SAMUM 2006. *Tellus* **61B**, 32–50.

Karyampudi, V. M., Palm, S. P., Reagen, J. A., Fang, H., Grant, W. B. and co-authors. 1999. Validation of the Saharan Dust Plume Conceptual Model Using Lidar, Meteosat, and ECMWF Data. *Bull. Am. Met. Soc.* **80**, 1045–1075.

Kaufman, Y. J., Koren, I., Remer, L. A., Tanré, D., Ginoux, P. and co-authors. 2005. Dust transport and deposition observed from the Terra-Moderate Resolution Imaging Spectroradiometer (MODIS) spacecraft over the Atlantic Ocean. *J. Geophys. Res.* **110**, D10S12, doi:10.1029/2003JD004436.

Kiefert, L., McTainsh, G. H. and Nickling, W. G. 1996. Sedimentological characteristics of Saharan and Australian Dusts. In: *The Impact of Desert Dust Across the Mediterranean* (eds. S. Guerzoni and R. Chester). Kluwer Academic Publishers, Dordrecht, 183–190.

Knippertz, P., Tesche, M., Heinold, B., Kandler, K., Toledano, C. and co-authors. 2011. Dust Mobilization and Aerosol Transport from West Africa to Cape Verde—A Meteorological Overview of SAMUM-2. *Tellus* **63B**, this issue.

Koren, I., Kaufman, Y. J., Washington, R., Todd, M. C., Rudich, Y. and co-authors. 2006. The Bodélé depression: a single spot in the Sahara that provides most of the mineral dust to the Amazon forrest. *Environ. Res. Lett.* **1**, 014005, doi:10.1088/1748-9326/1/1/014005.

Kretz, R. 1983. Symbols for rock-forming minerals. *Am. Mineral.* **68**, 277–279.

Mahowald, N. M., Yoshioka, M., Collins, W. D., Conley, A. J., Fillmore, D. W. and co-authors. 2006. Climate response and radiative forcing from mineral aerosols during the last glacial maximum, pre-industrial, current and doubled-carbon dioxide climates. *Geophys. Res. Lett.* **33**, L20705, doi:10.1029/2006GL026126.

McRae, G. J., Shair, F. H. and Seinfeld, J. H. 1981. Convective downmixing of plumes in a coastal environment. *J. Appl. Meteorol.* **20**, 1312–1324.

Middleton, N. J. and Goudie, A. S. 2001. Saharan dust: sources and trajectories. *Trans. Inst. Br. Geogr.* **26**, 165–181.

Moore, D. M. and Reynolds, R. C. J. 1997. *X-Ray Diffracton and the Identification and Analysis of Clay Minerals*. New York, Oxford University Press, Oxford.

Moulin, C., Dulac, F., Lambert, C. E., Chazette, P., Jankowiak, I. and co-authors. 1997. Long-term daily monitoring of Saharan dust load over ocean using Meteosat ISCCP-B2 data 2. Accuracy of the method and validation using Sun photometer measurements. *J. Geophys. Res.* **102**, 16959–16969.

Muhs, D. R., Budahn, J. R., Prospero, J. M. and Carey, S. N. 2007. Geochemical evidence for African dust inputs to soils of western Atlantic islands: Barbados, the Bahamas, and Florida. *J. Geophys. Res.* **112**, F02009, doi:10.1029/2005JF000445.

Nalli, N. R., Clemente-Colón, P., Morris, V., Joseph, E., Szczodrak, M. and co-authors. 2005. Profile observations of the Saharan air layer during AEROSE 2004. *Geophys. Res. Lett.* **32**, L05815, doi:10.1029/2004GL022028/.

Noll, K. E. and Fang, K. Y. P. 1989. Development of a dry deposition model for atmospheric coarse particles. *Atmos. Environ.* **23**, 585–594.

Osborne, S. R., Johnson, B. T., Haywood, J. M., Baran, A. J., Harrison, M. A. J., and co-authors. 2008. Physical and optical properties of mineral dust aerosol during the Dust and Biomass-burning Experiment. *J. Geophys. Res.* **113**, D00C03, doi:10.1029/2007JD009551.

Prospero, J. 1996. Saharan dust transport over the north Atlantic Ocean and Mediterranean: an overview. In: *The Impact of Desert Dust Across the Mediterranean* (eds. S. Guerzoni and R. Chester). Kluwer Academic Publishers, Dordrecht.

Prospero, J. M. 1999. Long-range transport of mineral dust in the global atmosphere: impact of African dust on the environment of the southeastern United States. *P. Natl. Acad. Sci. USA* **96**, 3396–3403.

Prospero, J. M. and Carlson, T. N. 1972. Vertical and areal distribution of Saharan dust over the western equatorial North Atlantic Ocean. *J. Geophys. Res.* **77**, 5255–5265.

Prospero, J. M., Glaccum, R. A. and Nees, R. T. 1981. Atmospheric transport of soil dust from Africa to South America. *Nature* **289**, 570–572.

Ratmeyer, V., Balzer, W., Bergametti, G., Chiapello, I., Fischer, G. and co-authors. 1999a. Seasonal impact of mineral dust on deep-ocean particle flux in the eastern subtropical Atlantic Ocean. *Mar. Geol.* **159**, 241–252.

Ratmeyer, V., Fischer, G. and Wefer, G. 1999b. Lithogenic particle fluxes and grain size distributions in the deep ocean off northwest Africa: Implications for seasonal changes of aeolian dust input and downward transport. *Deep-Sea Res. I* **46**, 1289–1337.

Reid, J. S., Kinney, J. E., Westphal, D. L., Holben, B. N., Welton, E. J. and co-authors. 2003. Analysis of measurements of Saharan dust by airborne and ground-based remote sensing methods during the Puerto Rico Dust Experiment (PRIDE). *J. Geophys. Res.* **108**, 8586, doi:10.1029/2002JD002493.

Rognon, P., Coudé-Gaussen, G., Revel, M., Grousset, F. and Pedemay, P. 1996. Holocene Saharan dust deposition on the Cape Verde Islands: sedimentological and Nd-Sr isotopic evidence. *Sedimentology* **43**, 359–366.

Schladitz, A., Müller, T., Nowak, A., Kandler, K., Lieke, K. and co-authors. 2011. In -situ aerosol characterization at Cape Verde. Part 1: particle number size distributions, hygroscopic growth and state of mixing of the marine and Saharan dust aerosol. *Tellus* **63B**, this issue.

Schütz, L., Jaenicke, R. and Pietrek, H. 1981. Saharan dust transport over the North Atlantic Ocean. *Geol. Soc. Am. Spec. Paper* **186**, 87–100.

Shao, Y. 2008. *Physics and Modelling of Wind Erosion.*, Springer, Dordrecht.

Środoń, J. and Eberl, D. D. 1980. The presentation of X-ray data for clay minerals. *Clay Minerals* **31**, 235–238.

Stuut, J.-B., Zabel, M., Ratmeyer, V., Helmke, P., Schefuss, E. and co-authors. 2005. Provenance of present-day eolian dust collected off NW Africa. *J. Geophys. Res.* **110**, D04202, doi:10.1029/2004JD005161.

Talbot, R. W., Harriss, R. C., Browell, E. V., Gregory, G. L., Sebacher, D. I. and co-authors. 1986. Distribution and geochemistry of aerosols in the Tropical North Atlantic Troposphere: relationship to Saharan Dust. *J. Geophys. Res.* **91**, 5173–5182.

Tanré, D., Haywood, J., Pelon, J., Léon, J. F., Chatenet, B. and co-authors. 2003. Measurement and modeling of the Saharan dust radiative impact: overview of the Saharan Dust Experiment (SHADE). *J. Geophys. Res.* **108**, 8574, doi:10.1029/2002JD003273.

Tegen, I. 2003. Modeling the mineral dust aerosol cycle in the climate system. *Quat. Sci. Rev.* **22**, 1821–1834.

Westphal, D. L., Toon, O. B. and Carlson, T. N. 1988. A Case Study of Mobilisation and Transport of Saharan Dust. *J. Atmos. Sci.* **45**, 2145–2175.

Zimmermann, F., Weinbruch, S., Schütz, L., Hofmann, H., Ebert, M. and co-authors. 2008. Ice nucleation properties of the most abundant mineral dust phases. *J. Geophys. Res.* **113**, D23204, doi:10.1029/2008JD010655.

Zipser, E. J., Twohy, C. H., Tsay, S.-C., Hsu, N. C., Heymsfield, G. M. and co-authors. 2009. The Saharan Air Layer and the Fate of African Easterly Waves—NASA's AMMA Field Study of Tropical Cyclogenesis. *Bull. Am. Met. Soc.* **90**, 1137–1156.

Supporting Information

Additional supporting information may be found in the online version of this article:

This electronic supporting information consists of two files containing raw X-ray diffraction count data of all samples measured in this work. Both files are tables with the single columns divided by a tabulator character. The first column contains the angle in $^\circ$ 2Θ, the following columns the raw counts. The file XRD_powder.txt contains the measurements of the randomly orientated filter samples for each single day. The column headers denote the date in 2008, for the exact sampling times refer to Table 1. For instrument parameters refer to Table 2, only samples marked with a + were measured with the Philips instrument. The file XRD_textured.txt contains the measurement of the textured sum samples of the meteorological periods. For details on sample preparation refer to text.

Please note: Wiley-Blackwell is not responsible for the content or functionality of any supporting materials supplied by the authors. Any queries (other than missing material) should be directed to the corresponding author for the article.